Nature Communications

https://doi.org/10.1038/s41467-026-75137-y

Article in Press

# Gas-phase unfolding assay rapidly predicts structure-function relationships in engineered antibodies with tuned flexibilities

Received: 22 August 2025

Accepted: 24 June 2026

Published online: 29 June 2026

Cite this article as: Villafuerte-Vega, R.C., Armbruster, M.R., Fisher, H. *et al.* Gas-phase unfolding assay rapidly predicts structure-function relationships in engineered antibodies with tuned flexibilities. *Nat Commun* (2026). https://doi.org/10.1038/s41467-026-75137-y

Rosendo C. Villafuerte-Vega, Michael R. Armbruster, Hayden Fisher, Isabel G. Elliott, H. T. Claude Chan, Tatyana Inzhelevskaya, C. Ian Mockridge, Christine A. Penfold, Patrick J. Duriez, Mark S. Cragg & Brandon T. Ruotolo

We are providing an unedited version of this manuscript to give early access to its findings. Before final publication, the manuscript will undergo further editing. Please note there may be errors present which affect the content, and all legal disclaimers apply.

If this paper is publishing under a Transparent Peer Review model then Peer Review reports will publish with the final article.

ARTICLE IN PRESS

© The Author(s) 2026. **Open Access** This article is licensed under a Creative Commons Attribution-NonCommercial-NoDerivatives 4.0 International License, which permits any non-commercial use, sharing, distribution and reproduction in any medium or format, as long as you give appropriate credit to the original author(s) and the source, provide a link to the Creative Commons licence, and indicate if you modified the licensed material. You do not have permission under this licence to share adapted material derived from this article or parts of it. The images or other third party material in this article are included in the article's Creative Commons licence, unless indicated otherwise in a credit line to the material. If material is not included in the article's Creative Commons licence and your intended use is not permitted by statutory regulation or exceeds the permitted use, you will need to obtain permission directly from the copyright holder. To view a copy of this licence, visit http://creativecommons.org/licenses/by-nc-nd/4.0/.

ARTICLE IN PRESS

# Gas-phase Unfolding Assay Rapidly Predicts Structure-Function Relationships in Engineered Antibodies with Tuned Flexibilities

Rosendo C. Villafuerte-Vega,[1,4] Michael R. Armbruster,[1] Hayden Fisher,[2,3] Isabel G. Elliott,[2] H.T. Claude Chan,[2] Tatyana Inzhelevskaya,[2] C. Ian Mockridge,[2] Christine A. Penfold,[2] Patrick J. Duriez,[2] Mark S. Cragg,[2] and Brandon T. Ruotolo[1]*

1 Department of Chemistry, University of Michigan, Ann Arbor, Michigan 48109, United States
2 Centre for Cancer Immunology, University of Southampton, Southampton, SO16 6YD, UK
3 Present Address: European Synchrotron Radiation Facility, Grenoble, Cedex 9, 38043, France
4 Present Address: Analytical Research & Development, Merck & Co., Inc., Rahway, NJ 07065, United States

* Correspondence to: bruotolo@umich.edu

ARTICLE IN PRESS

## ABSTRACT

Human (*h*)IgG2 monoclonal antibodies (mAbs) are potent agonists due, in part, to their ability to undergo disulfide shuffling within their hinge regions. Herein, we describe a rapid, sensitive, collision-induced unfolding (CIU) assay that possesses a predictive relationship between gas-phase protein unfolding and agonism in *h*IgG2 variants. Furthermore, our results highlight the significance of hinge engineering in tuning mAb structure-function relationships for the development of future biotherapeutics.

## INTRODUCTION

Monoclonal antibodies (mAbs) can elicit powerful effector mechanisms by mimicking endogenous ligands of immune cell surface receptors. Previous studies have demonstrated that immunomodulatory antibodies stimulate immune receptors in an isotype- and epitope-dependent manner.[1-3] For example, switching from human immunoglobulin G1 (*h*IgG1) or G4 (*h*IgG4) to a *h*IgG2 isotype confers FcγR-independent agonism to various anti-*h*CD40 mAbs by promoting *h*CD40 receptor clustering within the membrane that leads to enhanced downstream intracellular signaling.[3, 4] The unique ability of *h*IgG2 to augment receptor agonism is also observed in mAbs directed to other

ARTICLE IN PRESS

receptors[4,8] and is driven, in part, by its ability to undergo disulfide switching within its $C_H1$ and hinge regions, resulting in two isoforms: a flexible A-form (*h*IgG2A) and a rigid B-form (*h*IgG2B).[5, 6] These structural isoforms have demonstrated opposing immunostimulatory activity in murine models, where *h*IgG2A lacks activity and *h*IgG2B exhibits strong agonism.[1, 4] Building upon these observations, cysteine to serine (C/S) *h*IgG2B-like variants of ChiLob7/4 which retained a disulfide crossover between opposing heavy and light chains were shown to be less flexible, occupying reduced conformational space in solution.[7] Therefore, the mechanistic underpinnings of *h*IgG2B agonism can be partly explained by confined receptor mobility, leading to enhanced receptor clustering and immune activation.[8]

However, establishing a quantitative molecular explanation for the structural effects of C/S hinge engineering on *h*IgG2 agonism has been limited and time-consuming. Moreover, only $F(ab')_2$ fragments have routinely been structurally probed due to the inherent dynamism of full-length *h*IgGs.[7, 9] These limitations necessitate the development and validation of new, high-throughput methodologies capable of probing the structure-function relationships of full-length, hinge-engineered agonist mAbs. Herein, we describe a methodology that rapidly probes the impact of C/S hinge engineering on the structures of agonist mAbs in the gas-phase. We combine both ion mobility-mass spectrometry (IM-MS) and collision-induced unfolding (CIU) measurements to demonstrate that hinge disulfide modifications influence the structures and stabilities of full-length *h*IgG and $F(ab')_2$ scaffolds in a manner that strongly correlates with hinge flexibility and receptor agonism.

**RESULTS**

First, we examined how disulfide hinge variations affect the gas-phase compaction of various ChiLob7/4 C/S full-length *h*IgG2 variants.[7] This collapse is, in part, facilitated by the capacity of the IgG hinge to provide the necessary steric freedom for Fab and Fc domains to form compact structures

ARTICLE IN PRESS

ARTICLE IN PRESS

during nano-electrospray ionization (nESI).[10] Qualitatively, we observed that agonistic ChiLob7/4 variants (*h*IgG2 WT, C233S κC214S, C239S, and C232S κC214S) had broader $^{TW}\Omega_{N2}$ distributions than non-agonistic variants (*h*IgG1 WT and C232S + C233S), indicating a wider range of gas-phase structures (Supplementary Figs. 1a and b). Further comparison of centroid $^{TW}\Omega_{N2}$ values of these distributions revealed that agonistic variants had larger $^{TW}\Omega_{N2}$ values, indicating less gas-phase compaction. To support this conclusion, we leveraged Gaussian fitting to quantify the observed $^{TW}\Omega_{N2}$ distributions, focusing on charge states $22^+$ and $23^+$ given their normal, symmetric $^{TW}\Omega_{N2}$ distributions that better reflect native-like protein configurations.[11-13] Overall, our analysis revealed that non-agonistic variants adopt a narrower distribution of more compact conformations in the gas-phase, reflective of their more pliable hinge regions (Supplementary Fig. 1d). Most interestingly, the trends that we observe in centroid $^{TW}\Omega_{N2}$ and peak width values are predictive of agonism in the order of C232S + C233S < C233S κC214S < C239S ≅ C232S κC214S as described previously.[7]

We also detected similar trends in gas-phase compaction when analyzing $F(ab')_2$ fragments (Supplementary Fig. 2a). Agonistic variants occupied a bimodal distribution of $^{TW}\Omega_{N2}$ values, which indicated lesser degrees of compaction, while non-agonistic variants exhibited more unimodal distributions, especially for lower charge states (Supplementary Fig. 2b). Centroid $^{TW}\Omega_{N2}$ values for the more compact distributions in each variant further revealed an increase in $^{TW}\Omega_{N2}$ values in the order of C232S + C233S < C233S κC214S < C239S ≅ C232S κC214S (Supplementary Fig. 2c), which agreed with the $^{TW}\Omega_{N2}$ measurements of full-length *h*IgGs. Since $F(ab')_2$ fragments elicit the same activity as full-length *h*IgG2s,[4, 7] our IM-MS results provide strong evidence that variations in hinge flexibility modulate the gas-phase structures of ChiLob7/4 C/S variants in a manner that correlates with agonism.

Previous reports have detailed the potential of CIU-based assays to scrutinize mAb higher-order structure and stability.[14-18] However, prior CIU-based assays have not been used to either evaluate the C/S variants described here or predict mAb function. Since we observed that hinge flexibility modulates

ARTICLE IN PRESS

the gas-phase structures of ChiLob7/4 *h*IgG2 C/S variants, we speculated that their CIU profiles would be similarly differentiated. When subjecting full-length *h*IgG2 ions ($23^+$ to $25^+$) to CIU, we observed remarkably different unfolding patterns for *h*IgG2A, *h*IgG2B, and engineered mAbs (Supplementary Fig. 3). Differences appear at collision voltages (CVs) above 100 V, with agonistic variants accessing unfolded structures with higher ${}^{TW}\Omega_{N2}$ values than those of non-agonistic variants. In the CIU fingerprints of $24^+$ ions, for example, non-agonistic variants unfold to a third feature with a ${}^{TW}\Omega_{N2}$ below 98 $nm^2$, while agonistic variants predominantly transition to a more elongated fourth feature with a ${}^{TW}\Omega_{N2}$ above 100 $nm^2$ (Fig. 1a). Next, we performed a total difference analysis of CIU data utilizing a root-mean-square deviation (RMSD) approach (Fig. 1b). Comparing the CIU fingerprints of the non-agonistic variants to the highly agonistic C232S κC214S variant yielded RMSDs greater than ~32%. Comparisons to other agonistic variants, however, produced RMSDs lower than ~22%, emphasizing that the presence of a disulfide crossover causes agonistic variants to exhibit somewhat similar ${}^{TW}\Omega_{N2}$ distributions during CIU that can potentially inform candidate selection.

A detailed comparison of $CIU_{50}$ stability values revealed that non-agonistic variants produced larger $CIU_{50}$-1 values than agonistic variants (Fig. 1c). Within this scope, we noticed that a decrease in $CIU_{50}$-1 values correlated with an increase in agonism in the order of C232S + C233S < C233S κC214S < C239S ≅ C232S κC214S.[7] This gas-phase stability trend is likely influenced by the differing degrees of compaction experienced by each variant, where more compacted mAb structures develop increased energy barriers to unfolding.[11] As above, we observed that non-agonistic variants were structurally more compact than agonistic variants in the gas phase (Fig. 1d). Trends in gas-phase compaction, feature number, and $CIU_{50}$-1 were confirmed for similar *h*IgG2 variants derived from two further mAb: SAP9 (Figs. 1e-h) and Lob7/6 (Supplementary Figs. 4 a-d). Together, these data emphasize the broad applicability of CIU for identifying potentially agonistic antibodies based on quantifiable shifts in gas-phase stability.

ARTICLE IN PRESS

ARTICLE IN PRESS

CIU fingerprints for F(ab')$_2$ fragments (Supplementary Fig. 5) reveal differences reminiscent of our CIU results for full-length *h*IgGs, where we observed distinct features at higher CVs (Fig. 2a). A pairwise RMSD analysis of F(ab')$_2$ fragments revealed similar trends to those observed for full-length *h*IgGs (Fig. 2). For most F(ab')$_2$ samples, we observe comparable trends in gas-phase stability, where agonistic variants undergo CIU at lower CVs when compared to non-agonistic variants, and gas-phase stabilities are shifted in a manner that corresponds to both decreases in F(ab')$_2$ compaction and increases in mAb agonism (Fig. 2d). These trends were also validated across SAP9 (Fig 2e) and Lob7/6 (Supplementary Fig 4e) variants. Together, our full-length *h*IgG and F(ab')$_2$ data are predictive of mAb hinge flexibility and agonism. Importantly, the comparable trends in our rapidly-acquired CIU data for *h*IgG and F(ab')$_2$ constructs eliminate the need for F(ab')$_2$ fragment generation that is often needed to perform lower-throughput measurements that provide detailed assessments of mAb structure and flexibility.[7]

We also leveraged our CIU approach to study the structural effects of hinge disulfide engineering in another clinically relevant anti-4-1BB (*h*CD137) mAb, SAP1.3, which show the same trends in agonism for the C/S variants as ChiLob7/4, Lob7/6 and SAP9.[19] Two extra variants (C232S and C233S), engineered to be *h*IgG2A-like, were generated for this analysis. Data recorded for the $24^+$ charge state of SAP1.3 variants revealed CIU features that were similar to those of the ChiLob7/4 variants, where agonistic variants featuring a disulfide crossover readily transitioned to CIU features with $^{TW}\Omega_{N2}$ values above 101 nm$^2$ at higher CVs (Fig. 3a). As expected, an assessment of gas-phase stability revealed a decrease in $CIU_{50}$ values for the first CIU transition in a manner that correlates with an increase in $^{TW}\Omega_{N2}$ values for the compact features detected at low CV (Fig. 3b). Importantly, these results align with the trends we observed in *h*IgG2 C/S variants from three other tested mAb , highlighting that C/S engineering leads to generalizable changes in mAb structure and stability across constructs that have different receptor targets. To automate our approach, we leveraged the machine

ARTICLE IN PRESS

learning features of CIUSuite 3.0 to construct a two-state classifier capable of predicting mAb function (Fig. 3c).[20] Using this classification scheme, we were able to correctly identify both *h*IgG2A and *h*IgG2B isoforms with probability values greater than 80%.

Taken together, our findings represent an IM-MS/CIU assay capable of accurate predictions of mAb function *in vivo*. This is especially enabling, as CIU data can be collected in less than 30s and analyzed in an automated manner to enable mAb engineering campaigns.[21, 22] Using a series of 23 mAbs, including 19 *h*IgG2 C/S exchange variants, we showed that hinge disulfides modulate the gas-phase collapse and stability in a manner that correlates with agonistic activity. Our dataset includes over 300 CIU fingerprints collected across full-length *h*IgG and F(ab')$_2$ scaffolds of the anti-*h*CD40 mAbs ChiLob7/4 and Lob7/6, the anti-*h*OX40 mAb, SAP9, and the *h*CD137 mAb, SAP1.3, and a wide variety of C/S variants, indicating the robustness of the structural trends that form the foundation of our assay. Overall, our results establish a previously unknown connection between gas-phase mAb structures and their *in vivo* functions that can be broadly leveraged into high-throughput assays for the improved discovery of new pharmaceuticals.

ARTICLE IN PRESS

## METHODS

**Antibody Production and Purification.** Kabat numbering is utilized throughout the report. Anti-*h*CD40 ChiLob7/4 *h*IgG2 and Lob7/6 C/S exchange variants including C232S + C233S, C233S κC214S, C239S, and C232S κC214S were generated by site-directed mutagenesis in Chinese Hamster Ovary cells. They were subsequently purified by protein A affinity chromatography using a HiTrap MabSelect SuRe protein A column (Cytiva). ChiLob7/4 C232S + C233S, C233S κC214S, C232S κC214S, and all Lob7/6 mAbs received additional size exclusion chromatography purification using a HiLoad Superdex 200 pg 16/600 column (Cytiva). mAb were confirmed to be endotoxin low (<5 EU/mg) using an Endosafe PTS device (Charles River Laboratories) and aggregate-free (<1%) via high-

ARTICLE IN PRESS

performance liquid chromatography (HPLC) as described previously[4, 7] Anti-*h*CD137 SAP1.3 and anti-*h*OX40 SAP9 C/S exchange variants including C232S + C233S, C232S, C233S, C233S κC214S, C239S, and C232S κC214S were produced in a similar manner.[19] To generate F(ab')$_2$ fragments, each mAb was digested with IdeS (FabRICATOR, Genovis) at a 1 unit IdeS per 1 μg IgG ratio for 1 hour in TRIS NaCl buffer at 37°C. Full-length IgG and F(ab')$_2$ fragments were then desalted into 500 mM ammonium acetate (pH ~7.0) followed by another round of desalting into 200 mM ammonium acetate (pH ~7.0) using Micro Bio-Spin P-6 columns (Bio-Rad). Final concentrations were then measured by UV absorbance using a NanoDrop 2000c spectrophotometer (Thermo Fisher Scientific). Prior to MS analysis, samples were further diluted with 200 mM ammonium acetate to a final concentration of 0.5 to 5 μM.

ARTICLE IN PRESS

**Native Ion Mobility-Mass Spectrometry (IM-MS).** IM-MS experiments, which separate kinetically-trapped protein structures according to their size (using IM) and mass (by MS) on the millisecond timescale, were performed on a quadrupole-ion mobility-time-of-flight mass spectrometer (Q-IM-ToF-MS). SAP1.3 and ChiLob7/4 samples were analyzed on a Synapt G2 HDMS (Waters), while SAP9 and Lob7/6 samples were analyzed on a Waters Synapt G2-S equipped with a Gen3 SID device operating in flythrough mode.[23] Samples (3 μL) were transferred to gold-coated borosilicate capillaries (5-10 μm inner diameter, Harvard Apparatus) prepared in-house with a Sutter P-97 Micropipette Puller (Sutter Instrument) and Quorum SC7620 Mini Sputter Coater (Quorum Technologies), and ions were generated via static nano-electrospray ionization (nESI) using a NanoLockSpray source operated in positive mode. Settings throughout the instrument were adjusted to improve the desolvation and transmission of native-like protein ions without significant activation prior to IM separation: capillary voltage, 1.1 to 1.3 kV; source temperature, 25°C; sample cone, 25 to 50 V; extraction cone, 0 V; trap collision voltage (CV), 4 to 10 V; trap DC bias, 40 to 50 V; helium cell DC: 45 V; and IMS bias, 5 V. The backing pressure was set between 7.3 to 7.9 mbar (G2) or 5.0 to 5.4 mBar

ARTICLE IN PRESS

(G2-S) for improved ion transmission for all samples. The trap traveling-wave (TW) ion guide was pressurized to 5.2 x $10^{-2}$ mbar of argon gas. The helium cell flow rate was operated at 200 mL/min and pressurized to 1.4 x $10^{-3}$ mbar. The TWIM cell (a length of 0.254 m) was operated at 90 mL/min of nitrogen gas and pressurized to ~3.4 mbar. TWIM separation was achieved with a TW height and velocity of 40 V and 600 V, respectively. The ToF-MS was operated in the 1,000 to 12,000 *m/z* range in sensitivity mode at a pressure of 2.4 x $10^{-6}$ mbar. Mass calibration of the instrument from 100 to 10,000 *m/z* was performed using a solution of cesium iodide (100 mg/mL in 30% isopropanol). D, L polyalanine, bovine serum albumin, concanavalin A and alcohol dehydrogenase were prepared and used as collision cross section (${}^{TW}\Omega_{N2}$) calibrants to convert IgG and F(ab')$_2$ drift times into ${}^{TW}\Omega_{N2}$ values as described previously.[24] All data was collected over 200 drift bins with a scan time of 0.5 s for 1 min. Three technical IM-MS measurements were acquired for each sample. IM-MS spectra shown in this work were visualized with MassLynx v4.2 and DriftScope v3.0 software (Waters) and depicted using Adobe Illustrator.

**Collision-Induced Unfolding (CIU).** CIU experiments, where protein ions are subjected to collisional activation in the ion trap preceding the IM analyzer, and their CCSs are tracked as a function of CV, were performed using static spray nESI. Disulfide bond integrity is expected to be maintained across the activation energies required for unfolding.[25] Ions corresponding to a single charge state were selected using the high *m/z* quadrupole then subjected to collisions with argon gas in the trap TW ion guide prior to TWIM separation. Here, the trap CV was ramped from either 5 to 200 V in 5 V increments for full-length IgG or 4 to 140 V in 4 V increments for F(ab')$_2$ fragments to produce CIU data. The dwell time for each CV step was 12 s, and the scan time was 0.5 s. CIU method files and sample lists were automatically generated using an in-house python script (MethodEditor). Up to 20 functions (CV steps) were combined into a single .raw file, and three technical CIU replicates were acquired for each sample.

ARTICLE IN PRESS

ARTICLE IN PRESS

**IM-MS and CIU Data Processing and Analysis.** Deconvolution of mass spectra was achieved using UniDec software.[26] IM and CIU .raw files were processed using CIUSuite 3[20] which encodes both TWIMExtract (v1.6)[27] and IMSCal (v1.0)[24] for semi-automated drift time extractions and $^{TW}\Omega_{N2}$ calibrations, respectively. Specifically, drift time distributions were extracted over an *m/z* range that covers a single protein charge state and excludes any nearby contaminant ions. $^{TW}\Omega_{N2}$ values were determined using a calibration function that incorporates the operating conditions (TW height and velocity; TWIM cell length, pressure, and temperature) of the Synapt G2/G2-S instrument. Importantly, no unfolded protein calibrants were utilized to perform $^{TW}\Omega_{N2}$ calibrations.

Distributions of $^{TW}\Omega_{N2}$-calibrated IM data for individual charge states were fitted with a gaussian function to calculate centroid $^{TW}\Omega_{N2}$ and full width at half maximum (FWHM) values using Fityk curve fitting software.[28] Since IMSCal produces calibrated $^{TW}\Omega_{N2}$ values with a level of uncertainty, we estimated the total centroid $^{TW}\Omega_{N2}$ error (in nm$^2$) associated with three technical replicate measurements using the following equation:

$$error = \sqrt{\sigma^2 + \Omega_{N2}_error^2 + cal_rmse^2} \qquad (1)$$

where $\sigma$ is the standard deviation of technical replicate values, $\Omega_{N2}_error^2$ is the uncertainty of calibrated IgG or F(ab')$_2$ $^{TW}\Omega_{N2}$ values, and $cal_rmse^2$ is the $^{TW}\Omega_{N2}$ calibration root-mean-squared error (RMSE). Generally, we observed a % $^{TW}\Omega_{N2}$ calibration RMSE of less than 0.7%, and % uncertainties in IgG and F(ab')$_2$ $^{TW}\Omega_{N2}$ values were approximately 0.6 and 0.4%, respectively.

$^{TW}\Omega_{N2}$ calibrated CIU files were further processed using CIUSuite 3. Data were 2D smoothed using a Savitzky-Golay filter with a window size of 5 and 2 smooth iterations. CIU fingerprints were cropped in both $^{TW}\Omega_{N2}$ and CV axes for better visualization. Standard feature detection was performed using minimum feature length of 3 steps, an allowed width of 2.5 to 2.8 nm$^2$ in $^{TW}\Omega_{N2}$ axis units, and a maximum CV gap length of 2. $CIU_{50}$ values were then calculated using max centroiding mode with a

ARTICLE IN PRESS

ARTICLE IN PRESS

transition padding of 15 V and a maximum CV gap length of 2. By convention, $CIU_{50}$-1 refers to the $CIU_{50}$ value for the lowest energy transition observed in a given CIU dataset, with larger numbers assigned to the $CIU_{50}$ values extracted from successively higher-energy CIU transitions. Root-mean-square deviation (RMSD) analysis was performed using the compare function within CIUSuite 3. All CIU fingerprints shown are the average of three technical CIU replicates with replicate RMSD values of less than 8%. The classification algorithm within CIUSuite 3 was used to assemble and classify training and test (unknown) data sets, respectively.[29, 30] Classifiers were built in *All_Data* mode using three replicates for each class. The classifier discussed in Figure 3 was built using CIU data recorded for SAP1.3 C232S + C233S and C232S κC214S $24^+$ ions (n = 3) and tested using CIU data collected for C232S, C233S, C239S, C232S + C233S and C232S κC214S $24^+$ ions not included in the training dataset. The $24^+$ ion test data used for C232S, C233S, and C239S SAP1.3 variants were all quadrupole selected, whereas $24^+$ ions for C232S + C233S and κC214S data were extracted via software post-processing from full MS data files for classifier testing. All classification was performed using CCS-calibrated CIU data. Cross-validation was performed using a score tolerance of 0.02, and the cross-validation accuracy metric was used to choose the optimal classifier.

## DATA AVAILABILITY

The native IM-MS and CIU data generated in this study have been deposited in the Deep Blue Data (DBD), a service provided by the University of Michigan Library. DOI: https://doi.org/10.7302/w3mn-vv67. Source Data are provided with this paper.

## REFERENCES

1. Yu, X. et al. Complex Interplay between Epitope Specificity and Isotype Dictates the Biological Activity of Anti-human CD40 Antibodies. *Cancer Cell* **33**, 664-675.e664 (2018).
2. Beers, S.A., Glennie, M.J. & White, A.L. Influence of immunoglobulin isotype on therapeutic antibody function. *Blood* **127**, 1097-1101 (2016).

ARTICLE IN PRESS


3. Yu, X. et al. Isotype Switching Converts Anti-CD40 Antagonism to Agonism to Elicit Potent Antitumor Activity. *Cancer Cell* **37**, 850-866.e857 (2020).
4. White, A.L. et al. Conformation of the Human Immunoglobulin G2 Hinge Imparts Superagonistic Properties to Immunostimulatory Anticancer Antibodies. *Cancer Cell* **27**, 138-148 (2015).
5. Wypych, J. et al. Human IgG2 Antibodies Display Disulfide-mediated Structural Isoforms. *Journal of Biological Chemistry* **283**, 16194-16205 (2008).
6. Zhang, B., Harder, A.G., MConnelly, H.M., Maheu, L.L. & Cockrill, S.L. Determination of Fab-Hinge Disulfide Connectivityin Structural Isoforms of a Recombinant HumanImmunoglobulin G2 Antibody. *Analytical Chemistry* **82**, 1090-1099 (2010).
7. Orr, C.M. et al. Hinge disulfides in human IgG2 CD40 antibodies modulate receptor signaling by regulation of conformation and flexibility. *Science Immunology* **7** (2022).
8. Yu, X. et al. TNF receptor agonists induce distinct receptor clusters to mediate differential agonistic activity. *Communications Biology* **4** (2021).
9. Jay, J. et al. IgG Antibody 3D Structures and Dynamics. *Antibodies* **7**, 18 (2018).
10. Hansen, K. et al. A Mass-Spectrometry-Based Modelling Workflow for Accurate Prediction of IgG Antibody Conformations in the Gas Phase. *Angewandte Chemie* **130**, 17440-17445 (2018).
11. Hall, Z., Politis, A., Bush, M.F., Smith, L.J. & Robinson, C.V. Charge-state dependent compaction and dissociation of protein complexes: insights from ion mobility and molecular dynamics. *J Am Chem Soc* **134**, 3429-3438 (2012).
12. Zhong, Y., Han, L. & Ruotolo, B.T. Collisional and Coulombic Unfolding of Gas-Phase Proteins: High Correlation to Their Domain Structures in Solution. *Angewandte Chemie* **126**, 9363-9366 (2014).
13. Shelimov, K.B., Clemmer, D.E., Hudgins, R.R. & Jarrold, M.F. Protein Structure in Vacuo: Gas-Phase Conformations of BPTI and Cytochrome c. *J. Am. Chem. Soc.* **119**, 2240-2248 (1997).
14. Villafuerte-Vega, R.C. et al. Ion Mobility-Mass Spectrometry and Collision-Induced Unfolding of Designed Bispecific Antibody Therapeutics. *Anal Chem* **95**, 6962-6970 (2023).
15. Desligniere, E. et al. Combination of IM-Based Approaches to Unravel the Coexistence of Two Conformers on a Therapeutic Multispecific mAb. *Anal Chem* **94**, 7981-7989 (2022).
16. Tian, Y., Lippens, J.L., Netirojjanakul, C., Campuzano, I.D.G. & Ruotolo, B.T. Quantitative collision-induced unfolding differentiates model antibody–drug conjugates. *Protein Science* **28**, 598-608 (2019).
17. Vallejo, D.D. et al. Collision-Induced Unfolding Reveals Stability Differences in Infliximab Therapeutics under Native and Heat Stress Conditions. *Anal Chem* **93**, 16166-16174 (2021).
18. Zhao, R., Liu, N., Zheng, Z. & Li, G. Enhanced Stability Differentiation of Therapeutic Polyclonal Antibodies with All Ion Unfolding-Ion Mobility-Mass Spectrometry. *J Am Soc Mass Spectrom* **34**, 2289-2295 (2023).
19. Elliott, I.G. et al. Structure-guided disulfide engineering restricts antibody conformation to elicit TNFR agonism. *Nature Communications* **16**, 3495 (2025).
20. Jeon, C.K., Rojas Ramirez, C., Makey, D.M., Kurulugama, R.T. & Ruotolo, B.T. CIUSuite 3: Next-Generation CCS Calibration and Automated Data Analysis Tools for Gas-Phase Protein Unfolding Data. *Journal of the American Society for Mass Spectrometry* (2024).
21. D'Amico, C.I., Polasky, D.A., Steyer, D.J., Ruotolo, B.T. & Kennedy, R.T. Ion Mobility-Mass Spectrometry Coupled to Droplet Microfluidics for Rapid Protein Structure Analysis and Drug Discovery. *Analytical Chemistry* **94**, 13084-13091 (2022).


ARTICLE IN PRESS

ARTICLE IN PRESS

22. Juliano, B.R. et al. Development of an Automated, High-Throughput Methodology for Native Mass Spectrometry and Collision-Induced Unfolding. *Analytical Chemistry* **95**, 16717-16724 (2023).
23. Snyder, D.T., Panczyk, E.M., Somogyi, A., Kaplan, D.A. & Wysocki, V. Simple and Minimally Invasive SID Devices for Native Mass Spectrometry. *Analytical Chemistry* **92**, 11195-11203 (2020).
24. Richardson, K., Langridge, D., Dixit, S.M. & Ruotolo, B.T. An Improved Calibration Approach for Traveling Wave Ion Mobility Spectrometry: Robust, High-Precision Collision Cross Sections. *Anal Chem* **93**, 3542-3550 (2021).
25. Wei, B. et al. Added Value of Internal Fragments for Top-Down Mass Spectrometry of Intact Monoclonal Antibodies and Antibody–Drug Conjugates. *Analytical Chemistry* **95**, 9347-9356 (2023).
26. Marty, M.T. et al. Bayesian Deconvolution of Mass and Ion Mobility Spectra: From Binary Interactions to Polydisperse Ensembles. *Analytical Chemistry* **87**, 4370-4376 (2015).
27. Haynes, S.E. et al. Variable-Velocity Traveling-Wave Ion Mobility Separation Enhancing Peak Capacity for Data-Independent Acquisition Proteomics. *Analytical Chemistry* **89**, 5669-5672 (2017).
28. Wojdyr, M.J. Fityk: A general-purpose peak fitting program. *J. Appl. Cryst.* **43**, 1126-1128 (2010).
29. Polasky, D.A., Dixit, S.M., Fantin, S.M. & Ruotolo, B.T. CIUSuite 2: Next-Generation Software for the Analysis of Gas-Phase Protein Unfolding Data. *Anal Chem* **91**, 3147-3155 (2019).
30. Polasky, D.A., Dixit, S.M., Vallejo, D.D., Kulju, K.D. & Ruotolo, B.T. An Algorithm for Building Multi-State Classifiers Based on Collision-Induced Unfolding Data. *Anal Chem* **91**, 10407-10412 (2019).

ARTICLE IN PRESS

ARTICLE IN PRESS

**Funding:** This work was supported by the National Science Foundation (2304961 to B.T.R.), the National Institutes of Health (R01-GM095832 to B.T.R.), and Cancer Research UK (Award number DRCDDRPGMApr2020\100005 to M.S.C.).

**Author contributions:** B.T.R. and M.S.C. conceived the study and supervised the project. H.F., I.G.E., H.T.C.C., T.I., C.I.M., C.A.P., and P.J.D. prepared the samples, validated the results, and contributed to the study conceptualization and methodology. R.V.V. and M.R.A. performed the experiments, validated the results, and analyzed the data.

**Competing Interests:** The authors declare no competing interests.

ARTICLE IN PRESS

ARTICLE IN PRESS

## Figure Legends:

**Fig. 1:** CIU analysis scrutinizes the effects of hinge disulfide variation on the structure and stability of ChiLob7/4 (**a – d**) and SAP9 *h*IgG2 variants (**e – h**). **a,** Averaged CIU fingerprints for the $24^+$ charge state of ChiLob7/4 *h*IgG2 variants, where up to four features are observed. **b,** Pairwise RMSD comparisons of C232S κC214S with other variants. **c,** Left: representative plots showing sigmoidal fitting of the first CIU transition using CIUSuite 3.[20] Right: $CIU_{50}$ values for the first transition shown as mean ± s.d. **d,** $^{TW}\Omega_{N2}$ values of the first CIU feature shown as mean ± propagated $^{TW}\Omega_{N2}$ error (see Methods). **e,** Averaged CIU fingerprints for the $24^+$ charge state of SAP9 *h*IgG2 variants. **f,** Pairwise RMSD comparisons of C232S κC214S with other variants. **g,** $CIU_{50}$ values for the first CIU transition. Data are shown as mean ± s.d. **h,** $^{TW}\Omega_{N2}$ values of feature 1 shown as mean ± propagated $^{TW}\Omega_{N2}$ error. All data were collected from n = 3 technical CIU replicates per sample. Source data are provided as a Source Data file.

**Fig. 2:** CIU analysis scrutinizes the effects of hinge disulfide variation on the structure and stability of ChiLob7/4 (**a – d**) and SAP9 *h*IgG2 F(ab')$_2$ variants (**e – h**). **a,** Averaged CIU fingerprints for the $21^+$ charge state of ChiLob7/4 F(ab')$_2$ fragments, where up to five features are observed. **b,** Pairwise RMSD comparisons of C232S κC214S with other variants. **c,** $CIU_{50}$ values for the CIU transition between features two and three. Data are shown as mean ± s.d. **d,** $^{TW}\Omega_{N2}$ values of features one (left) and two (right) shown as mean ± propagated $^{TW}\Omega_{N2}$ error. **e,** Averaged CIU fingerprints for the $21^+$ charge state of SAP9 *h*IgG2 F(ab')$_2$ fragments. **f,** Pairwise RMSD comparisons of C232S κC214S with other variants. **g,** $CIU_{50}$ values for the first CIU transition between features 2 and 3. Data are shown as mean ± s.d. **h,** $^{TW}\Omega_{N2}$ values of features one (left) and two (right) shown as mean ± propagated $^{TW}\Omega_{N2}$ error. All data were collected from n = 3 technical CIU replicates per sample. Source data are provided as a Source Data file.

ARTICLE IN PRESS

**Fig. 3:** CIU rapidly classifies C/S variants of the *h*CD137 *h*IgG2 mAb, SAP1.3. **a,** Averaged CIU fingerprints for the $24^+$ charge state of each variant, where up to four features are observed. **b,** Top: $^{TW}\Omega_{N2}$ values of the first CIU feature shown as mean ± propagated $^{TW}\Omega_{N2}$ error. Bottom: $CIU_{50}$ values for the first CIU transition shown as mean ± s.d. **c,** CIU-based classification workflow: **i,** assignment of CIU training data sets to classes, **ii,** selection of voltage steps better suited for distinguishing classes; five voltages were selected (red, data are shown as mean ± s.d.), **iii,** cross-validation analysis tests the accuracy of the classification model, **iv,** linear discriminate analysis enables sorting of training data sets into two classes, **v,** replicates not used as training data are correctly assigned to their respective classes. Probabilities are shown as mean ± s.d. of classification results for technical replicates. All data were collected from n = 3 technical CIU replicates per sample. Source data are provided as a Source Data file.

ARTICLE IN PRESS

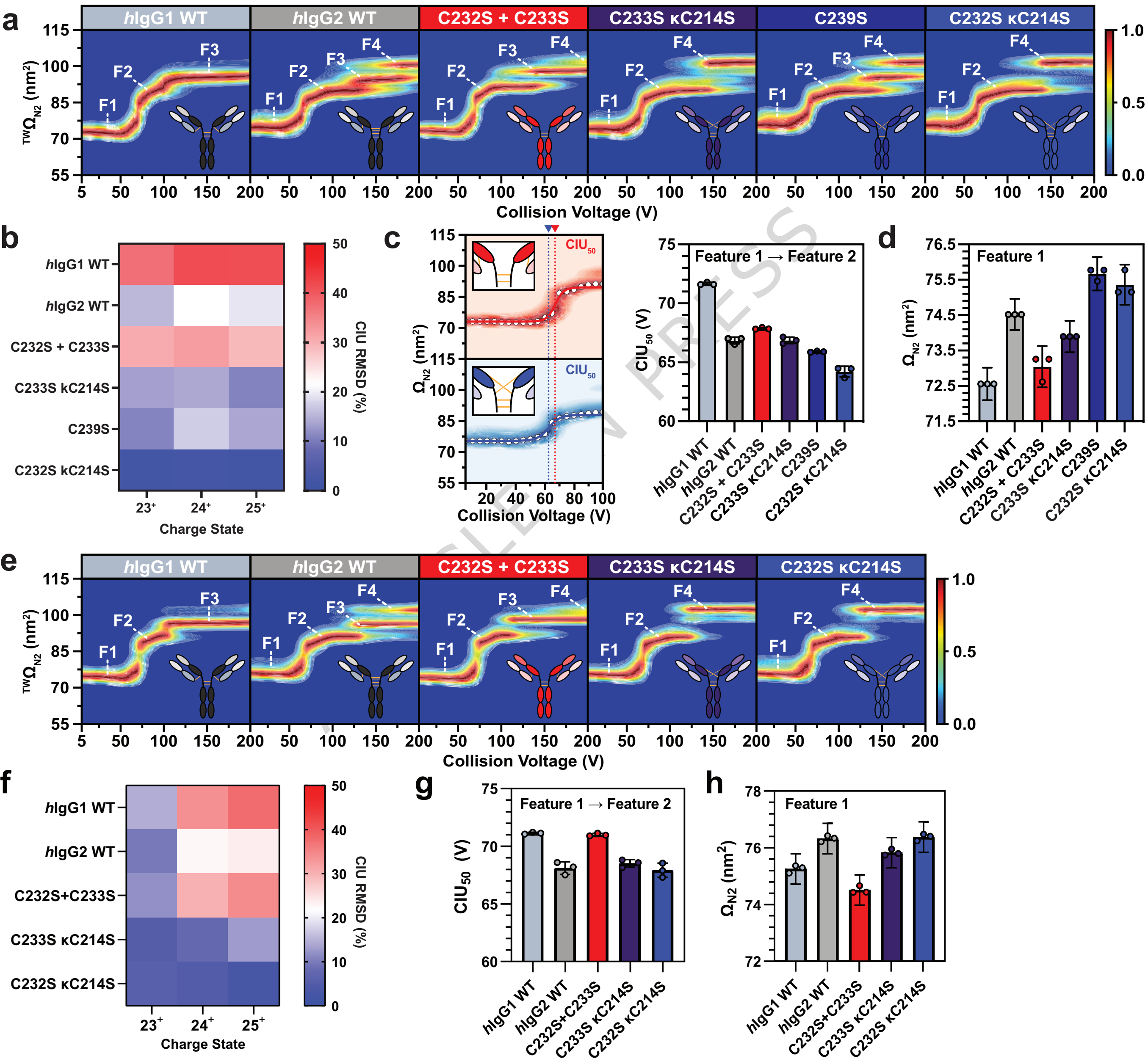

ARTICLE IN PRESS

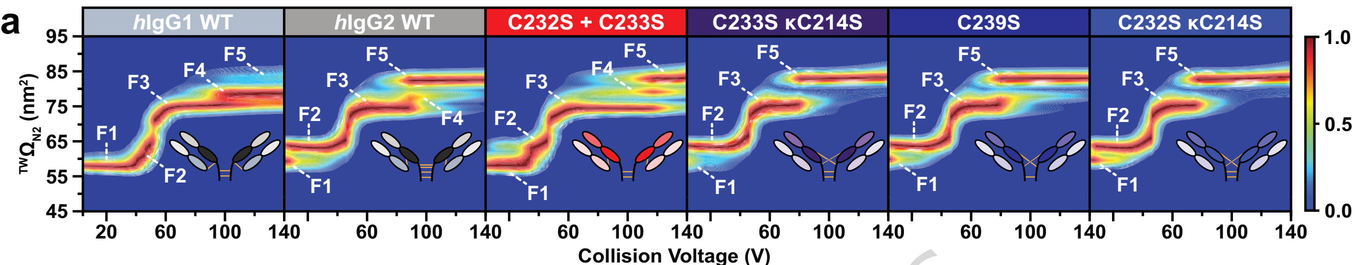


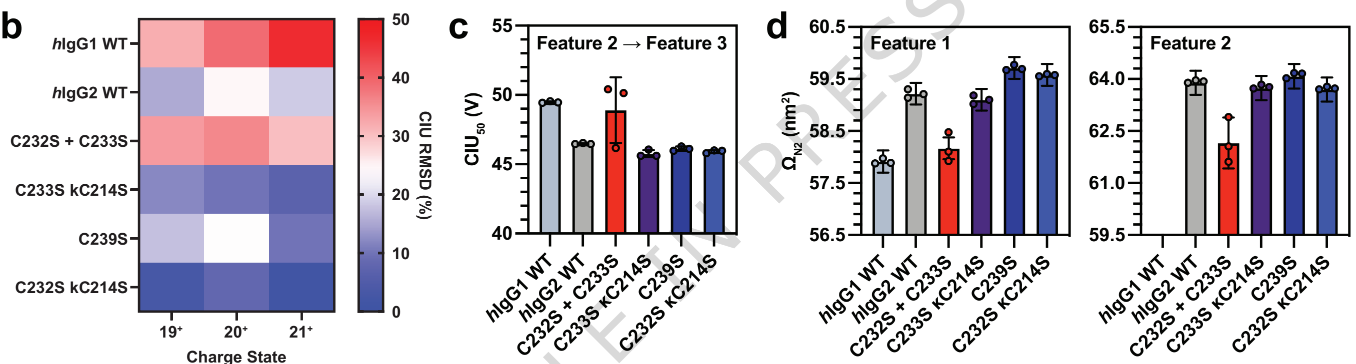


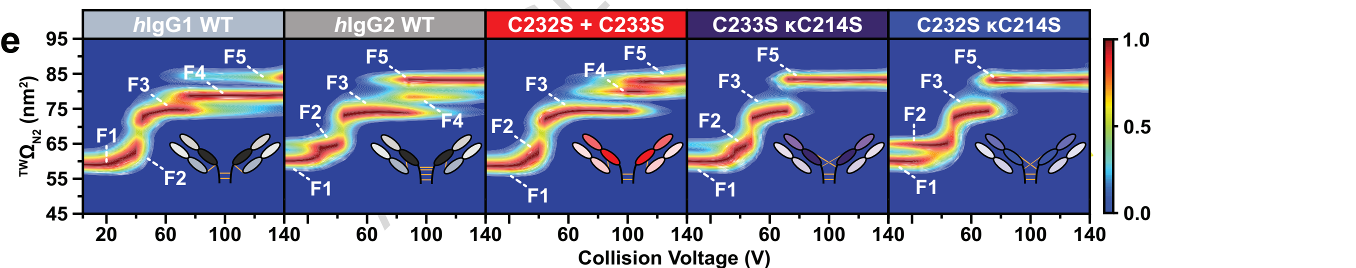


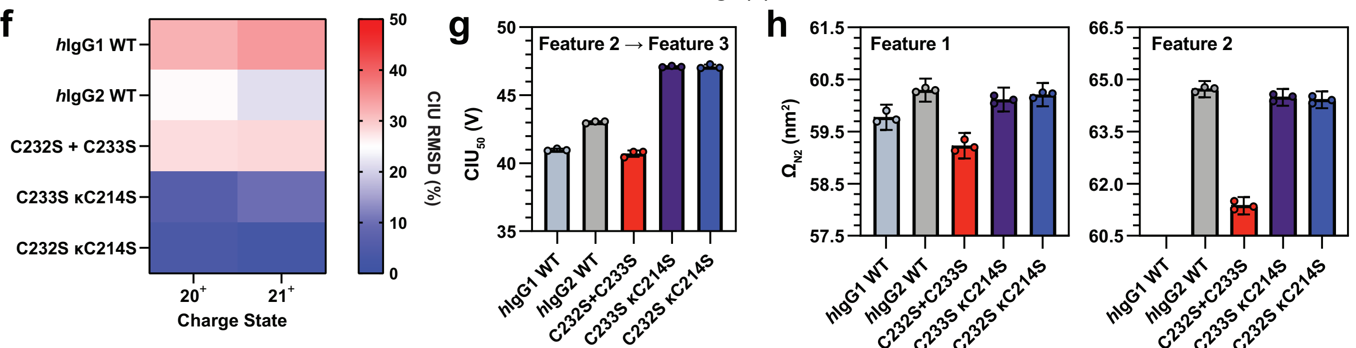

ARTICLE IN PRESS